Short Iterative Lanczos Integration in Time-Dependent Equation-of-Motion Coupled-Cluster Theory

Brandon C. Cooper,[†] Lauren N. Koulias,[‡] Daniel R. Nascimento,[¶] Xiaosong Li,[*,‡] and A. Eugene DePrince III[*,†]

†*Department of Chemistry and Biochemistry, Florida State University, Tallahassee, FL 32306-4390*

‡*Department of Chemistry, University of Washington, Seattle, WA 98195*

¶*Department of Chemistry, The University of Memphis, Memphis, TN, 38152*

E-mail: xsli@uw.edu; adeprince@fsu.edu

Abstract

A time-dependent (TD) formulation of equation-of-motion coupled-cluster (EOM-CC) can provide excited-state information over an arbitrarily-wide energy window with a reduced memory footprint relative to conventional, frequency-domain EOM-CC theory. However, the floating-point costs of the time-integration required by TD-EOM-CC are generally far larger than those of the frequency-domain form of the approach. This work considers the potential of the short iterative Lanczos (SIL) integration scheme [*J. Chem. Phys.* **1986**, *85*, 5870-5876] to reduce the floating-point costs of TD-EOM-CC simulations. Low-energy and K-edge absorption features for small molecules are evaluated using TD-EOM-CC with single and double excitations, with the time-integrations carried out via SIL and fourth-order Runge-Kutta (RK4) schemes. Spectra derived from SIL- and RK4-driven simulations are nearly indistinguishable, and, with an appropriately-chosen subspace dimension, the SIL requires far fewer floating-point operations than are required by RK4. For K-edge spectra, SIL is the more efficient scheme by an average factor of 7.2.

Introduction

Time-domain methods for the *ab initio* description of light-matter interactions are increasingly popular,[1–17] as they offer several advantages over more familiar frequency-domain approaches to the excited-state problem. The primary benefit of working directly in the time domain is that such approaches offer natural descriptions of a variety of processes that cannot be directly modeled within a linear response framework, including high harmonic generation,[5,9,10,18] ultrafast charge[19,20] and energy migration[21,22] and laser induced ionization.[23–28] Second, time-domain methods offer the practical advantage that they can be used to generate spectral information over an arbitrarily-wide energy range through analysis of only a few time-domain signals.[29] Frequency-domain approaches, on the other hand, generally involve the iterative diagonalization of a sizeable matrix, which can become challenging

when large numbers of roots are desired. When applying frequency-domain techniques to broad spectral features in systems with high densities of states, one must contend with both potential stability issues associated with standard iterative diagonalization schemes, as well as with the storage requirements associated with such algorithms. This latter issue can be particularly problematic in the case of many-body electronic structure methods.[30]

Despite their nice properties, time-domain methods are not a panacea; they are subject to their own limitations, the most obvious of which is the long simulation time required to fully resolve closely-spaced spectral features. For example, a typical simulation may require the numerical integration of the time-dependent Schrödinger equation over tens of thousands of time steps. Consequently, the most promising strategies to reduce the cost of a time-dependent calculation are to either reduce the length of a simulation required to achieve a given spectral resolution, or to reduce the cost of the time integration itself. Total simulation length can be minimized through advanced signal processing techniques such as the Padé approximation to the Fourier transform.[31–33] Reducing the cost of the time evolution itself requires the careful selection of an appropriate numerical integrator.

Propagation schemes for many-body wave function expansions often rely on simple numerical integration techniques,[32,34–39] namely the fourth-order Runge-Kutta (RK4) scheme, despite the fact that RK4 is not symplectic (meaning that stable RK4-based integrations may require small step sizes). More sophisticated symplectic integrators[40–42] have been applied in the context of both time-dependent truncated configuration interaction (CI)[14] and time-dependent CC theory.[43–45] The algebraic diagrammatic construction (ADC) community also has a long history[19–22,46,47] of performing time integrations according to the short iterative Lanczos (SIL) scheme originally proposed by Park and Light.[48] In the SIL approach, an approximation to the Hamiltonian, $\mathbf{H}_k$, is constructed according to the Lanczos procedure, and exact quantum dynamics are approximated by the dynamics associated with $\mathbf{H}_k$. This approximation is valid for only a short time after which a new approximate Hamiltonian must be constructed. In practice, the cost of repeatedly constructing $\mathbf{H}_k$ can be far less than

evaluating the dynamics with the exact Hamiltonian and a standard integration scheme such as RK4.

In this work, we explore the efficacy of the SIL procedure in the context of the moment-based formulation of time-dependent (TD) equation-of-motion coupled-cluster (EOM-CC)[49–52] theory developed in Ref. 35. Our SIL protocol is formulated according to a standard Lanczos procedure for Hermitian matrices, despite the fact that the EOM-CC Hamiltonian is non-Hermitian. While an asymmetric SIL scheme could be formulated in a way that accounts for this non-Hermiticity,[53] we demonstrate that the standard SIL algorithm provides a sufficiently accurate description of the TD-EOM-CC dynamics relevant to the evaluation of both low-energy and K-edge absorption features.

Theory

Time-Dependent Equation-of-Motion Coupled-Cluster Theory

It has been shown[35] that the EOM-CC oscillator strength function, $f(\omega)$, can be obtained from the real part of a lineshape function, $I_\xi(\omega)$, as

$$f(\omega) = \frac{2}{3}\omega \sum_\xi \mathscr{R}\{I_\xi(\omega)\} \tag{1}$$

with $I_\xi(\omega)$ defined by the Fourier transform

$$I_\xi(\omega) = \int_{-\infty}^{\infty} dt\, e^{-i\omega t} \left\langle \phi_0 \right| (1 + \hat{\Lambda}) \bar{\mu}_\xi e^{i\bar{H}_N t} \bar{\mu}_\xi \left| \phi_0 \right\rangle . \tag{2}$$

Here, $|\phi_0\rangle$ represents a reference configuration (which, in this work, is taken to be a determinant of generalized Hartree-Fock [GHF] spinors), $\hat{\Lambda}$ is the coupled-cluster (CC) de-excitation operator, $\bar{\mu}_\xi$ is the ξ-component ($\xi \in x, y, z$) of the similarity transformed dipole operator

$$\bar{\mu}_\xi = e^{-\hat{T}} \hat{\mu}_\xi e^{\hat{T}} \tag{3}$$

and $\bar{H}_N$ is the normal-ordered similarity-transformed Hamiltonian

$$\bar{H}_N = e^{-\hat{T}} \hat{H} e^{\hat{T}} - E_{\mathrm{CC}} \tag{4}$$

In Eqs. 3 and 4, the symbol $\hat{T}$ represents the cluster operator, and E_{CC} is the energy associated with the ground-state CC wavefunction. In this work, the ground state is treated at the CC with single and double excitations (CCSD)[54] level of theory, so the cluster and de-excitation operators take the form

$$\hat{T} = \sum_{ia} t_i^a \hat{a}_a^\dagger \hat{a}_i + \frac{1}{4} \sum_{ijab} t_{ij}^{ab} \hat{a}_a^\dagger \hat{a}_b^\dagger \hat{a}_j \hat{a}_i \tag{5}$$

and

$$\hat{\Lambda} = \sum_{ia} \lambda_a^i \hat{a}_i^\dagger \hat{a}_a + \frac{1}{4} \sum_{ijab} \lambda_{ab}^{ij} \hat{a}_i^\dagger \hat{a}_j^\dagger \hat{a}_b \hat{a}_a \tag{6}$$

respectively. Here $\hat{a}^\dagger$ and $\hat{a}$ represent second-quantized creation and annihilation operators, and the labels i/j and a/b refer to orthonormal spinors that are occupied and unoccupied in the reference determinant, respectively.

In order to evaluate the right-hand-side of Eq. 2 at all times, t, we first introduce time-dependent left- and right-hand CC dipole functions, which, in this work, are expanded in the basis of singly- and doubly-substituted configurations as

$$\langle \tilde{M}_\xi(t)| = \langle \phi_0| \big(\widetilde{m}_0 + \sum_{ia} \widetilde{m}_a^i \hat{a}_i^\dagger \hat{a}_a + \frac{1}{4} \sum_{ijab} \widetilde{m}_{ab}^{ij} \hat{a}_i^\dagger \hat{a}_j^\dagger \hat{a}_b \hat{a}_a \big), \tag{7}$$

and

$$|M_\xi(t)\rangle = \big(m_0 + \sum_{ia} m_i^a \hat{a}_a^\dagger \hat{a}_i + \frac{1}{4} \sum_{ijab} m_{ij}^{ab} \hat{a}_a^\dagger \hat{a}_b^\dagger \hat{a}_j \hat{a}_i \big) |\phi_0\rangle, \tag{8}$$

respectively. Initial values of the time-dependent $\tilde{m}$- and m-amplitudes at time $t = 0$ are defined according to

$$\langle \tilde{M}_\xi(0)| = \langle \phi_0| \, (1 + \hat{\Lambda}) \bar{\mu}_\xi \tag{9}$$

and

$$|M_\xi(0)\rangle = \bar{\mu}_\xi \, |\phi_0\rangle \tag{10}$$

We note that $\langle \tilde{M}_\xi(t)|$ and $|M_\xi(t)\rangle$ span the same space as the left- and right-hand eigenfunctions of the similarity-transformed Hamiltonian that one would encounter at the EOM-CC with single and double excitations (EOM-CCSD) level of theory. As such, given a CCSD treatment of the ground state, oscillator strengths obtained from Eq. 1 will be equivalent to those obtained from a frequency-domain EOM-CCSD calcluation.

Given these left- and right-hand dipole functions, the right-hand side of Eq. 2 takes the form of a moment autocorrelation function

$$I_\xi(\omega) = \int_{-\infty}^{\infty} dt \, e^{-i\omega t} \, \langle \tilde{M}_\xi(0)|M_\xi(-t)\rangle \tag{11}$$

and it becomes clear that knowledge of the right-hand moment function at all times is required to evaluate the lineshape and oscillator strength functions. The time-evolution of $|M_\xi(t)\rangle$ is governed by the the time-dependent Schrödinger equation

$$i\frac{\partial}{\partial t}\mathbf{m}_\xi(t) = \bar{\mathbf{H}}_N \mathbf{m}_\xi(t) \tag{12}$$

where $\mathbf{m}_\xi(t)$ and $\bar{\mathbf{H}}_N$ are the vector and matrix representations of $|M_\xi(t)\rangle$ and $\bar{H}_N$, respectively. We note that TD-EOM-CC conserves time-reversal symmetry [*i.e.*, $\mathbf{m}_\xi(t) = \mathbf{m}^*_\xi(-t)$], and, as a result Eq. 12 need only be integrated over positive (or negative) times. This integration can be carried out using a variety of standard numerical integration techniques, including short iterative Lanczos scheme outlined in the following subsection.

Short Iterative Lanczos Integration

Given that the dimension of $\bar{\mathbf{H}}_N$ is generally too large to allow for its full diagonalization, the integration of Eq. 12 can be carried out using either explicit [20–22,30,32,35,46–48,55–60]

or implicit[55,56] numerical integrators that involve the repeated evaluation of matrix-vector products of the form $\boldsymbol{\sigma} = \bar{\mathbf{H}}_N \mathbf{m}_\xi(t)$. At the TD-EOM-CCSD level of theory, the number of floating-point operations involved in evaluating this matrix-vector product increases with the sixth power of the size of the system. As such, the repeated construction of σ-vectors is by far the most time-intensive step of a TD-EOM-CC simulation, and any significant reduction in the number of required σ-vector evaluations will greatly enhance the efficiency of the approach. Here, we present the general working equations for the SIL integration scheme (unmodified from Ref. 48), which can achieve exactly that aim.

The essence of the SIL approach is the estimation of exact quantum dynamics via the dynamics associated with an approximate Hamiltonian ($\mathbf{H}_k$), which is constructed according to the Lanczos algorithm. The evolution of a compact representation of the wave function using $\mathbf{H}_k$ is far less computationally demanding than the propagation of the full wave function using the exact Hamiltonian. However, $\mathbf{H}_k$ only provides an accurate approximation to $\bar{\mathbf{H}}_N$ (and thus an accurate representation of the dynamics) for a limited number of time steps, at which point the Lanczos procedure must be repeated. Even accounting for the repeated generation of the approximate Hamiltonian, the SIL method generally will require many times fewer σ-vector evaluations than are required by RK4.

The Lanczos algorithm generates an approximation of a given input matrix (*i.e.*, $\bar{\mathbf{H}}_N$), resulting in a tridiagonal matrix of the form

$$\mathbf{H}_k = \begin{bmatrix} \alpha_0 & \beta_1 & 0 & \cdots & 0 & 0 \\ \beta_1 & \alpha_1 & \beta_2 & \cdots & 0 & 0 \\ 0 & \beta_2 & \alpha_2 & \cdots & 0 & 0 \\ \vdots & \vdots & \vdots & \ddots & \vdots & \vdots \\ 0 & 0 & 0 & \cdots & \alpha_{k-2} & \beta_{k-1} \\ 0 & 0 & 0 & \cdots & \beta_{k-1} & \alpha_{k-1} \end{bmatrix} \tag{13}$$

Here, the label k refers to the dimension of the Lanczos subspace, as generated by the

algorithm below, and the coefficients of the approximate Hamiltonian are defined by

$$\alpha_k = \boldsymbol{\sigma}_k^\dagger \mathbf{a}_k \tag{14}$$

and

$$\beta_k = ||\mathbf{w}_{k-1}|| \tag{15}$$

Here, the vectors $\mathbf{a}_k$ and $\boldsymbol{\sigma}_k$ represent the Lanczos vectors and their corresponding sigma-vector products, respectively. The procedure is seeded with normalized $\mathbf{m}_\xi(t{=}0)$:

$$\mathbf{a}_0 = \mathbf{m}_\xi(t)/||\mathbf{m}_\xi(t)|| \tag{16}$$

which is used to generate the initial σ-vector

$$\boldsymbol{\sigma}_0 = \bar{\mathbf{H}}_N \mathbf{a}_0 \tag{17}$$

The first diagonal coefficient of $\mathbf{H}_k$, α_0 is simply the expectation value of this operator with respect to $\mathbf{a_0}$

$$\alpha_0 = \boldsymbol{\sigma}_0^\dagger \mathbf{a}_0 \tag{18}$$

and $\mathbf{w}_0$ is defined by

$$\mathbf{w}_0 = \boldsymbol{\sigma}_0 - \alpha_0 \mathbf{a}_0 \tag{19}$$

Subsequent elements of the approximate Hamiltonian (α_m and β_m, for $m = 1, ..., k-1$) are generated via

$$\beta_m = ||\mathbf{w}_{m-1}|| \tag{20}$$

$$\mathbf{a}_m = \frac{\mathbf{w}_{m-1}}{\beta_m} \tag{21}$$

$$\boldsymbol{\sigma}_m = \bar{\mathbf{H}}_N \mathbf{a}_m \tag{22}$$

$$\alpha_m = \boldsymbol{\sigma}_m^\dagger \mathbf{a}_m \tag{23}$$

$$\mathbf{w}_m = \boldsymbol{\sigma}_m - \alpha_m \mathbf{a}_m - \beta_m \mathbf{a}_{m-1} \tag{24}$$

In standard implementations of the Lanczos procedure, the coefficients α and β are assumed to be real-valued. Because the EOM-CC Hamiltonian is non-Hermitian we lift this restriction, allowing for α coefficients to become complex along with the Lanczos vectors; β coefficients, however, will remain real-valued as they are defined by a Euclidean norm.

Once $\mathbf{H}_k$ has been constructed, a compact representation of the moment function within the Krylov subspace is defined

$$\mathbf{c}(t) = \begin{bmatrix} 1 \\ 0 \\ 0 \\ \vdots \end{bmatrix} \tag{25}$$

and evolved according to the Schrödinger equation

$$\frac{\partial \mathbf{c}(t)}{\partial t} = -i\mathbf{H}_k \mathbf{c}(t). \tag{26}$$

Because $\mathbf{H}_k$ is so compact, the dynamics within the subspace can be evaluated exactly according to

$$\mathbf{c}(t + dt) = \exp(-i\mathbf{H}_k dt)\mathbf{c}(t), \tag{27}$$

and the time-evolved subspace representation of the moment function can then be transformed back into the original Hilbert space according to

$$\mathbf{m}_\xi(t + dt) = \mathbf{A}_k \mathbf{c}(t + dt) \tag{28}$$

The matrix $\mathbf{A}_k$, which translates the time-evolved dynamics in the subspace back into the

original basis, is constructed from the Lanczos vectors $\mathbf{a}_k$ as

$$\mathbf{A}_k = [\mathbf{a}_0\mathbf{a}_1\mathbf{a}_2...\mathbf{a}_{k-1}] \tag{29}$$

In this way, $\mathbf{m}_\xi(t)$ is evolved in an inexpensive way for as many time steps as possible, while monitoring the magnitude of the last element of $\mathbf{c}(t+dt)$ as a gauge of the fitness of $\mathbf{H}_k$. Once $|c_{k-1}(t+dt)|$ exceeds 10^{-8}, t is updated ($t \leftarrow t+dt$), a new Lanczos subspace is generated (seeded by $\mathbf{a}_0 = \mathbf{m}_\xi(t)/||\mathbf{m}_\xi(t)||$), and the subspace vector is reset according to Eq. 25 for subsequent time evolution. This process continues until the desired number of time steps have been evaluated.

Computational Details

All geometries were optimized at the CCSD/aug-cc-pVTZ level of theory using the Psi4 package.[61] All time-domain calculations were carried out using a development version of the Chronus Quantum software package.[62] Low-energy spectra were derived from the discrete Fourier transform (FT) of dipole autocorrelation functions, which were taken from simulations with a total time of 1350 a.u. ($\approx$ 32 fs) and time steps of 0.05 a.u. ($\approx 1.2 \times 10^{-3}$ fs). K-edge calculations involved shorter simulations (500 a.u. or $\approx$ 12 fs) and smaller time steps (0.01 a.u. or $\approx 2.4 \times 10^{-4}$ fs). Because of the small time step necessary to resolve K-edge features, these spectra were obtained using the Padé approximation to the FT, which has much better convergence properties than the discrete FT itself. In principle, a Padé-based analysis could be applied to the low-energy spectra as well, but we elect to perform the discrete FT in this case because the Padé approximation can produce spurious features when applied to dense spectral regions. All spectra were artificially broadened using a Lorentzian line shape with a full width at half maximum of 0.2 eV. Benchmark calculations comparing the relative efficiencies of RK4 and SIL integrations as a function of the Lanczos dimension were performed using the cc-pVDZ basis set.[63] K-edge spectra were also generated using a

larger basis set (aug-cc-pVTZ[64]) and compared to experimentally obtained spectra.

Results and Discussion

The SIL-based TD-EOM-CC simulations described in this section consider the accuracy and efficiency of that integration scheme over a range of Lanczos subspace dimensions (k=5–50). Our goal is to identify a globally optimal subspace dimension that balances not only the accuracy and floating-point cost of the approach, but also its memory footprint, as increases in the subspace dimension translate into increases in the storage requirements of the TD-EOM-CC procedure as a whole. An RK4-based procedure requires the storage of only four copies of the moment-function amplitudes, whereas SIL will require a number of copies of these amplitudes that slightly exceeds the Lanczos subspace dimension, k. Hence, a choice of $k = 40$ in SIL carries a 10-fold increase in the storage requirements for the amplitudes, relative to RK4. In this case, the storage of the amplitudes could begin to rival the storage of the electron repulsion integrals, provided some tensor factorization strategy (*e.g.*, density fitting[65,66]) has been applied to that quantity. Consequently, minor improvements to the efficiency of SIL gained by a choice of large k may be outweighed by the increased storage requirements of the algorithm. Moreover, by limiting the Lanczos subspace dimension, we can hopefully reduce the occurrence of spurious features, known as ghost states,[67] that can emerge with large, over-converged Lanczos spaces.

As discussed above, the floating-point cost of a TD-EOM-CC simulation is linked to the total number of σ-vector evaluations required by the chosen integration scheme. Here, we explore how the Lanczos dimension employed within SIL relates to the number of σ-vector evaluations, while also monitoring the errors in computed spectra incurred through the use of the SIL integrator, as opposed to RK4. As an error metric, we define the percent error in

a computed spectrum as

$$\% \text{ error} = \frac{\int' |f_{\text{SIL}}(\omega) - f_{\text{RK4}}(\omega)| d\omega}{\int' f_{\text{RK4}}(\omega) d\omega} \times 100\% \tag{30}$$

where $f_{\text{SIL}}(\omega)$ and $f_{\text{RK4}}(\omega)$ represent oscillator strengths [Eq. 1] generated via SIL or RK4 integration, respectively, and the primes indicate that the integration is over some specified spectral region(s). For example, we separately consider the efficacy of SIL for low-energy (*i.e.*, 0–25 eV) and K-edge features, where the relevant frequency range at the K-edge depends upon the molecule of interest. In this analysis, for the K-edges in nitrogen, oxygen, and carbon, we consider the ranges 402–409 eV, 528–542 eV, and 292–295 eV, respectively. The number of σ-vector evaluations and percent errors for all of the benchmark simulations discussed below are tabulated in the Supporting Information.

Figure 5(a) illustrates the total number of σ-vector evaluations (red squares) required for generating low-energy (0–25 eV) spectra for several small open- and closed-shell molecules (H_2O, N_2, NH_3, CH_3, NO, and OH), using RK4 and SIL with Lanczos dimensions varying from 5 to 50. All calculations were carried out within the cc-pVDZ basis set, using a total simulation time of 1350 a.u. and a time step of 0.05 a.u., and the number of σ-vector evaluations have been averaged over simulations involving each molecule and each of the three cartesian components of the dipole function. Based on the total simulation time and time step, an RK4-based simulation requires 108,000 σ-vector evaluations. As can be seen in Fig. 5(a), SIL significantly reduces the number of σ-vector evaluations required for a given calculation, provided that the SIL subspace dimension is greater than five. For subspace dimensions k=10 and k=50, for example, the number of σ-vector evaluations are reduced by factors of 2.1 and 3.7, respectively. For the smallest subspace considered (k=5), we find only a small reduction in the number of σ-vector evaluations, on average, with some molecules (NO, H_2O, and OH) actually requiring more σ-vector evaluations within the SIL scheme. Also depicted in Fig. 5(a) is the average number of time steps that elapse between successive

$\mathbf{H}_k$ builds (blue circles). As the subspace dimension k increases, we observe a near-linear increase in the time for which the dynamics associated with $\mathbf{H}_k$ are reliable.

Figure 5(b) depicts the average percent error in the spectra obtained from SIL-based calculations, with RK4-derived spectra serving as reference values. The data indicate that the relative error between spectra generated by RK4 and SIL integration is generally small, provided that the subspace size exceeds k=5. Beyond k=5, the average percent error ranges from as large as 2.1% for k=10 to a minimum value of 0.1% at k=50, and we note that only modest improvements are observed beyond k=20, which has associated with it an average percent error equal to 0.5%. From these data, we conclude that a reasonable choice of subspace size that balances accuracy, floating-point costs, and memory requirements is k=20.

Figure 2 compares spectra generated via RK4 and SIL (with a subspace dimension k=20) over the range for which the percent error was evaluated. Visual inspection of the data reveals that both propagators yield indistinguishable spectra on this scale. As such, we have also included in Fig. 2 the deviation between the spectra (green dashed lines), and we only find one instance in which they differ by as much as 0.005; note that the the maximum feature in each spectrum scaled to one. For the case of H_2O, we have also calculated differences in the peak positions predicted by SIL- and RK4-based simulations. For all six features depicted in Fig. 2(e), these integrators yield peak positions that differ by less than 0.01 eV.

The number of σ-vector evaluations required for the evaluation of K-edge spectra is depicted in Fig. 3(a), along with the average number of time steps over which the approximate Hamiltonian, $\mathbf{H}_k$ provides reasonable dynamics. The associated average percent errors are illustrated in Fig. 3(b). Here, we consider the same basis set and molecules considered in the analysis above, and the total simulation time and time step were reduced to 500 a.u. and 0.01 a.u., respectively. With these parameters, an RK4-based simulation requires 200000 σ-vector evaluations. In contrast to the case of low-energy spectra, K-edge simulations performed using SIL with any subspace size (including k=5) are dramatically more efficient

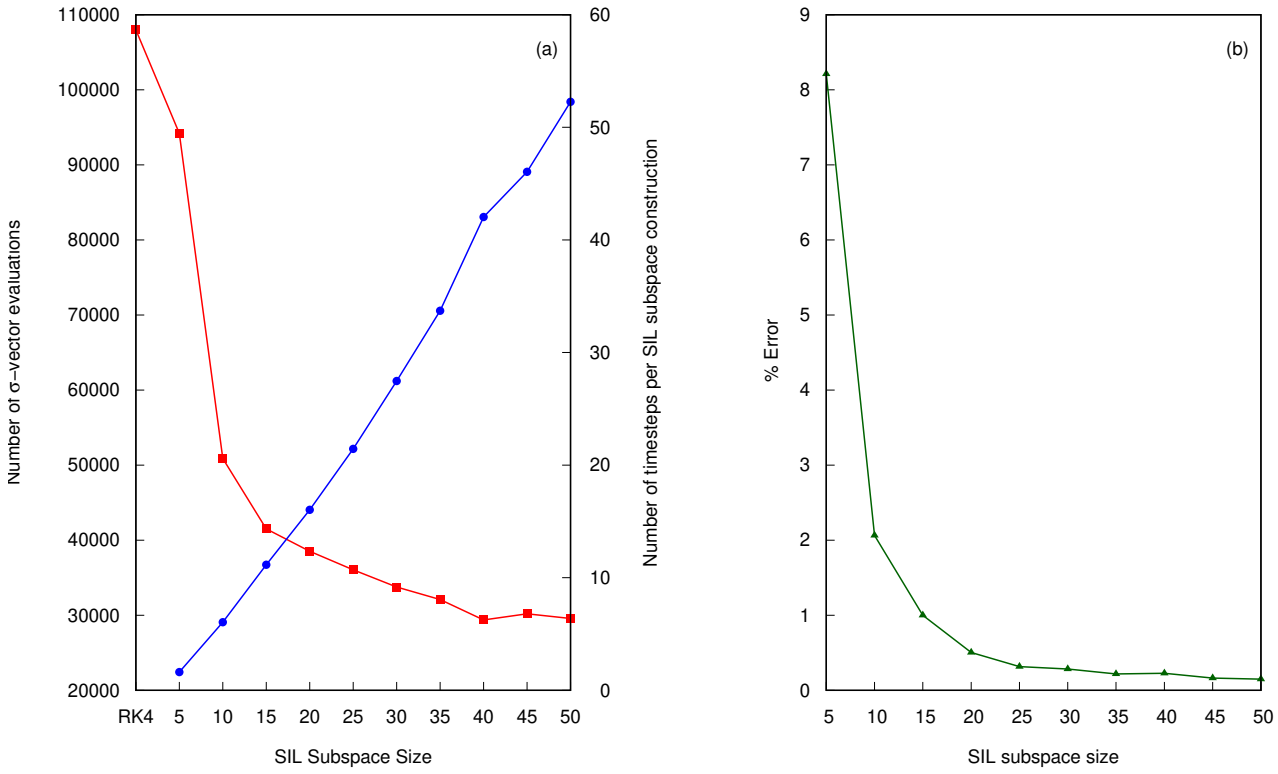

Figure 1: (a) The total number of σ-vector evaluations required (red squares) for RK4- and SIL-based TD-EOM-CC simulations of low-energy spectral features and the average number of time steps over which the approximate Hamiltonian ($\mathbf{H}_k$) provides reliable dynamic (blue circles), averaged over the set of test molecules and the three cartesian components of the dipole function. (b) The average percent error in the spectra derived from SIL integration, relative to those from RK4-based calculations.

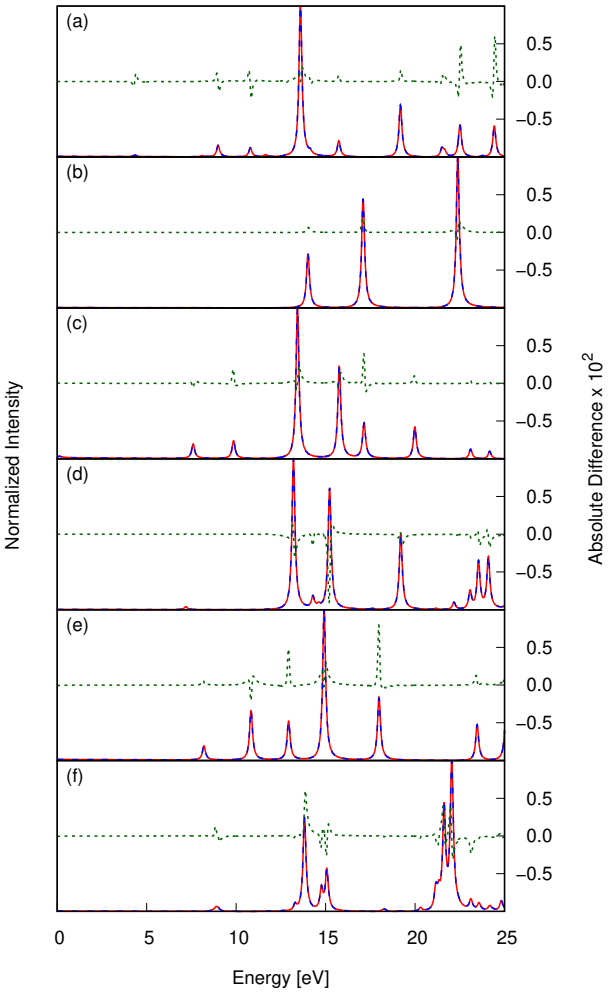

Figure 2: Low-energy spectra derived from the RK4- (solid red curves) and SIL-based (dashed blue curves) simulations of (a) OH (b) N_2 (c) NH_3 (d) CH_3 (e) H_2O (f) NO. Deviations between SIL- and RK4-derived spectra are indicated by the dashed green curves.

than simulations performed using RK4, with the greatest performance advantages of SIL occurring for $k \geq 10$. Simulations involving k=10 and k=50 require 9.6 and 17.9 fewer σ-vector evaluations than are required by RK4, respectively. Figure3(b) provides the average percent error for each SIL subspace size, again with the RK4-derived spectra serving as a reference. As in the case of low-energy spectra, the smallest subspace size (k=5) leads to the largest error, and only modest improvements are observed beyond k=20. The percent errors are generally larger for K-edge simulations than for simulations of the low-energy spectra, by roughly an order of magnitude, but, for $k \geq 20$, the average percent error never exceeds 4.1%. An analysis of the peak positions for the oxygen K-edge in H_2O suggests that this error derives from differences in the maximum heights of the peaks in the oscillator strength functions, as opposed to shifts in the peak positions; SIL and RK4-based predictions of the position of the two features at the oxygen K-edge in H_2O differ by only 0.01 eV. From these data, we again conclude that a reasonable choice of subspace size is k=20. In this case, SIL reduces the number of σ-vector evaluations required by RK4, on average, by a factor of 13.6.

Figure 4 directly compares K-edge spectra generated via RK4 and SIL (with a subspace dimension k=20), and once again, the spectra are difficult to distinguish visibly in most cases. The spectra are normalized such that the largest features in the K-edge region are one. We find that the deviations between SIL- and RK4-derived spectra (green dashed lines) can be roughly 10 times larger than in the case of the low-energy spectra considered above, but the largest errors observed are still quite small (with a maximum difference of roughly 0.06). As mentioned already, for the case of the oxygen K-edge in H_2O, the predicted positions for the two peaks illustrated in Fig. 4(e) differ by only 0.01 eV.

To this point, all computations have considered only modest basis sets (*i.e.*, cc-pVDZ), which may be too small for reliable estimates of excitation energies, particularly at the K-edge. Here, we assess the efficiency and accuracy of SIL-based integration for K-edge spectroscopy in a larger basis set (aug-cc-pVTZ), with the Lanczos dimension set at the optimal value determined via our benchmark analysis (k=20). Table 1 provides experimentally-

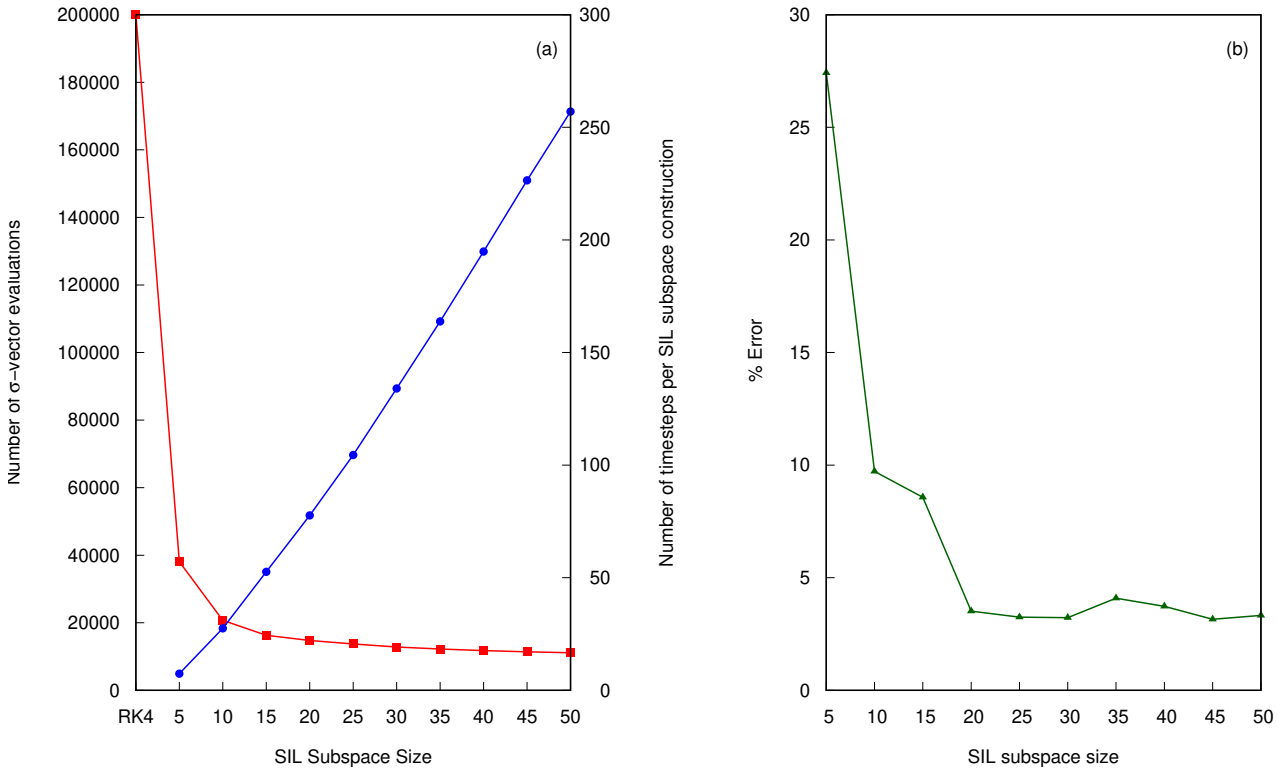

Figure 3: (a) The total number of σ-vector evaluations required (red squares) for RK4- and SIL-based TD-EOM-CC simulations of K-edge spectral features and the average number of time steps over which the approximate Hamiltonian ($\mathbf{H}_k$) provides reliable dynamic (blue circles), averaged over the set of test molecules and the three cartesian components of the dipole function. (b) The average percent error in the spectra derived from SIL integration, relative to those from RK4-based calculations.

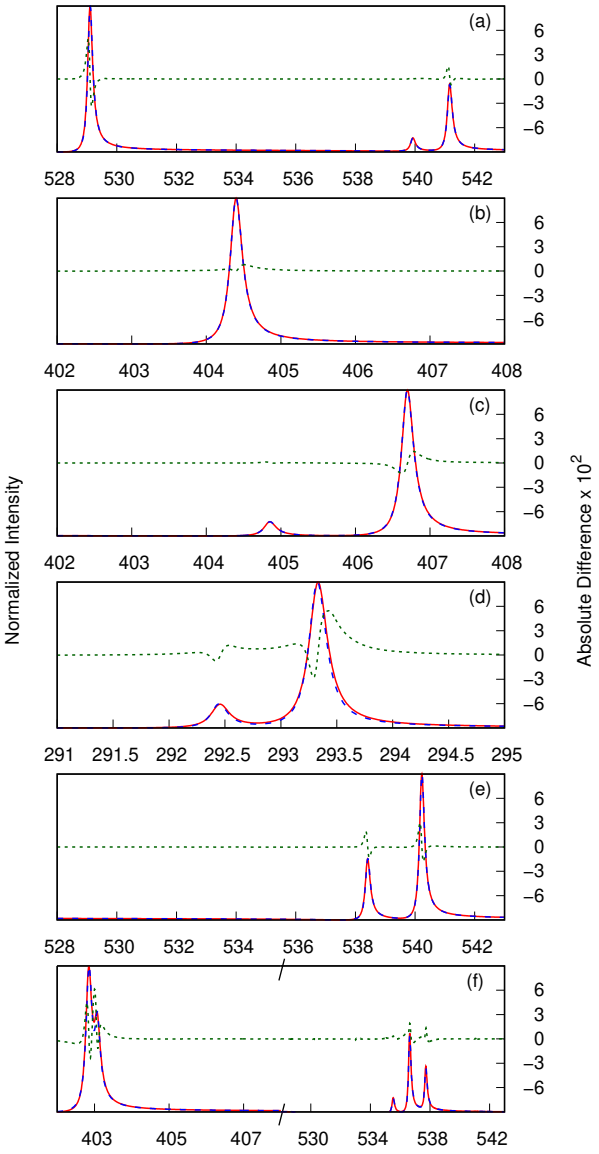

Figure 4: K-edge regions from the RK4(solid red line), SIL(dashed blue line) and the difference between them(dashed green line) for (a) OH (b) N_2 (c) NH_3 (d) CH_3 (e) H_2O (f) NO.

obtained K-edge features for the same small molecules above, as well the error in computed values at the TD-EOM-CCSD/aug-cc-pVTZ level of theory. Peak labels are taken from experiment,[68–73] and assignments of simulated peaks were made based on the symmetry of the lineshape function and the proximity of a given peak to the experimentally obtained one. Also provided are the number of σ-vector evaluations required for a TD-EOM-CCSD simulation, averaged over the three cartesian components of the dipole moment autocorrelation function. Using the same integration parameters used to generate the K-edge spectra above, an RK4-based calculation would require 200000 σ-vector evaluations per simulation. For the molecules we consider, SIL propagation improves upon this number by a factor of roughly four to nine, with an average improvement of 7.2x. Here, the worst-case acceleration is observed for OH, in which case SIL involves an average of 48253 σ-vector evaluations per simulation. The average performance enhancement (7.2x) is somewhat smaller than was observed in the cc-pVDZ basis (13.6x), but we can nonetheless conclude that SIL provides a significant computational advantage over less sophisticated integration schemes in both basis sets. As for the accuracy of the simulations, we find that the majority of the K-edge features predicted by TD-EOM-CCSD deviate from experimentally obtained features by less than 1.5 eV, with a worst-case deviation of 2.01 eV (for the 1s$\rightarrow$3p(a_1/b_1) transition in the water molecule), and, overall, the mean unsigned error in all features is only 1.15 eV. These values are consistent with the accuracy of TD-EOM-CCSD K-edge spectra reported previously for other small closed-[32,44] and open-shell[44] molecules. We note that, sub-eV accuracy can be achieved via the inclusion of triple excitations, which is easily done in time-independent EOM-CC calculations,[44] but which presents more of a computational challenge within a time-dependent EOM-CC framework. We also stress that the roughly 1 eV errors we observe pertain to K-edge features of second-row atoms. EOM-CCSD has been demonstrated to display similar accuracy at the sulfur K-edge,[74] but for heavier atoms, EOM-CCSD results in larger errors. For example, at the xenon K-edge in XeF_2, four-component EOM-CCSD, including the Gaunt interaction, results in a roughly 40 eV error, relative to experiment

(which translates into a 0.1% error in this case).[75]

Table 1: Experimentally-obtained K-edge features (eV) and errors in computed K-edge features (eV), along with the average number of σ-vector evaluations required for SIL simulations for each molecule.

	σ	transition	exp.	error
OH	48253	1s$\rightarrow$ 2p	525.80[69]	0.26
NO	27093	N 1s$\rightarrow$ 2pπ^*	399.70[70]	0.40
		O 1s$\rightarrow$ 2pπ^*	532.70[70]	1.13
N_2	25273	1s$\rightarrow$ 2pπ_g	401.00[71]	0.66
		1s$\rightarrow$ 3sσ_g	406.10[71]	1.45
		1s$\rightarrow$ 3pπ_u	407.00[71]	1.41
NH_3	22367	1s$\rightarrow$ 3s(a_1)	400.66[72]	0.96
		1s$\rightarrow$ 3p(e)	402.33[72]	0.96
		1s$\rightarrow$ 3p(a_1)	402.86[72]	1.53
		1s$\rightarrow$ 4s(a_1)	403.57[72]	1.70
		1s$\rightarrow$ 3p(e)	404.15[72]	1.91
CH_3	18453	1s$\rightarrow$ 2p	281.35[73]	0.26
H_2O	25847	1s$\rightarrow$ 3s	534.00[72]	1.35
		1s$\rightarrow$ 3p(b_2)	535.90[72]	1.24
		1s$\rightarrow$ 3p(a_1/b_1)	537.00[72]	2.01
MUE				1.15

The data presented above demonstrate that SIL-derived TD-EOM-CC spectra closely reproduce those from RK4-based simulations for both open- and closed-shell species and for both valence and core-level transitions. This result is somewhat surprising, as SIL was originally formulated for non-Hermitian Hamiltonians, and the similarity-transformed Hamiltonian is not Hermitian. One possible explanation for this excellent performance is that, for the systems that we have explored, $\bar{\mathbf{H}}_N$ is "close-enough" to Hermitian for the procedure to work. To test this hypothesis, we consider additional far-from-equilibrium geometries of a water molecule, within the cc-pVDZ basis. For this study, we consider spectra along a single bond stretch coordinate, varying one O–H bond length, while holding the other O–H bond length and the H–O–H bond angle fixed at values of 1.0 Å and 104.5°, respectively. Table 2 provides the percent error in the oscillator strength functions and the maximum errors in the peak locations for SIL-derived spectra, using RK4-based results as a reference. We find that the percent error for low-energy features increases slightly with increasing bond length, but

the errors remain low (the maximum percent error is 1.1%). We also evaluated the deviations between peak locations from SIL- and RK4-based simulations, and the maximum error we encountered was only 0.01 eV. For K-edge features, the percent error in the oscillator strength function is comparable to the average values presented in Fig. 3(b), and we find no clear trend in these values with increasing bond lengths. As in the case of low-energy features, the maximum error in the K-edge peak locations is only 0.01 eV. These data suggest that SIL remains a reliable choice of integrator when simulating far-from-equilibrium TD-EOM-CC spectra.

Table 2: Percent error in the oscillator strength function and maximum errors in peak locations (eV) for SIL-derived low-energy and K-edge features of H_2O along a single O–H bond stretch coordinate (Å).

	% error		max peak error	
bond length	low-energy	K-edge	low-energy	K-edge
1.0	0.5	4.1	0.00	0.01
1.5	0.6	4.7	0.01	0.01
2.0	0.6	5.4	0.01	0.01
2.5	1.1	4.5	0.01	0.01

Conclusions

We have explored the utility of the short iterative Lanczos integration scheme in the context of moment-based time-dependent equation-of-motion coupled-cluster theory. With a suitably-chosen Lanczos dimension, the SIL scheme can be as much as an order of magnitude more efficient than a simpler numerical integration protocol based on, for example, the RK4 approach. We validated the SIL procedure by evaluating both low-energy (0–25 eV) and K-edge absorption features in a variety of small molecules and found that SIL-derived spectra are nearly indistinguishable from those derived from RK4. This result is somewhat surprising, as SIL was originally formulated for Hermitian Hamiltonians, whereas the EOM-CC Hamiltonian is not Hermitian. Interestingly, we have found that the SIL scheme closely

reproduces spectra obtained from RK4-based simulations even in cases where we expect the similarity-transformed Hamiltonian to be significantly non-Hermitian (*e.g.*, at far-from-equilibrium geometries in H_2O). When combined with advanced signal processing techniques (*e.g.*, the Padé approximation to the discrete FT), the floating-point cost of a simulation of K-edge spectra, for example, can be reduced by more than an order of magnitude, relative to a naive TD-EOM-CC simulation. Even so, such simulations are still expensive, requiring tens of thousands of σ-vector builds, and may become impractical for large molecules. In that case, these techniques could easily be combined with other approaches that exploit the sparsity of the Hamiltonian (*e.g.*, core-valence separation[76–79] or local correlation techniques) in order to expand their utility.

We reiterate that the TD-EOM-CC approach described in this work is a moment-based one,[35] and we note that a complementary time-domain approach to EOM-CC theory could be developed in which the system is exposed to a time-dependent external perturbation (*e.g.*, an oscillating electric field), and spectral information can subsequently be extracted from the time evolution of observables such as the dipole moment.[80,81] Such an approach, which we refer to as field-driven TD-EOM-CC, is, in principle, more robust than the moment-based one in that it can naturally describe non-linear effects. Nevertheless, several factors potentially complicate the use of this complementary field-driven form of TD-EOM-CC theory, particularly with a Lanczos-based integration scheme. First, the SIL procedure works under the assumption that the Hamiltonian is time-independent, so SIL-accelerated dynamics could only be realized when the time-dependent external perturbation goes to zero (*e.g.*, after the system has been perturbed). Second, because EOM-CC is not a Hermitian theory, evaluating the time-dependent dipole moment requires knowledge of both the left- and right-hand wave functions. For this reason, correct SIL-based dynamics would likely require the use of an asymmetric Lanczos tridiagonalization procedure.[82] Finally, one should recall that neither RK4 nor SIL are structure conserving, and, while they appear to be reliable within the context of moment-based TD-EOM-CC theory, it could be preferable to employ

a suitable symplectic integrator[43–45] for field-driven TD-EOM-CC dynamics.

Lastly, we note that the moment-based formalism we employ derives[30,44] from the sum-over-states form of the frequency-dependent dipole polarizability,[83] which is not size-extensive.[84] As a result, TD-EOM-CC is also not strictly size extensive, but it does avoid the spurious poles discussed in Ref. 84. Fortunately, multiple studies have demonstrated the accuracy of moment-based TD-EOM-CC relative to conventional EOM-CC for both linear absorption spectra[35,44] and rotatory strengths,[30] so it would appear that any size-extensivity error is not problematic, at least in small molecules. Nonetheless, one should be aware of this issue.

Supporting Information

The number of σ-vector evaluations and the percent error in the oscillator strength functions associated with simulations of low-energy and K-edge spectra for all molecules considered in this study.

Acknowledgments

This work was supported by the U.S. Department of Energy, Office of Science, Basic Energy Sciences, under Award LAB 17-1775, as part of the Computational Chemical Sciences Program. LK is thankful for the fellowship support from the MolSSI software institute. The development of the time-dependent method is funded by the National Science Foundation (CHE-1856210). The development of the Chronus Quantum open source software package is supported by the National Science Foundation (OAC-1663636).

This work was supported by the U.S. Department of Energy, Office of Science, Basic Energy Sciences, under Award LAB 17-1775, as part of the Computational Chemical Sciences Program. L.K. is grateful for the fellowship support from the MolSSI software institute. The development of the time-dependent method is funded by the National Science Foundation

(CHE-1856210). The development of the Chronus Quantum open source software package is supported by the National Science Foundation (OAC-1663636).

References

(1) Li, X.; Govind, N.; Isborn, C.; DePrince, A. E.; Lopata, K. Real-Time Time-Dependent Electronic Structure Theory. *Chemical Reviews* **2020**, *120*, 9951–9993.

(2) Schlegel, H. B.; Smith, S. M.; Li, X. Electronic Optical Response of Molecules in Intense Fields: Comparison of TD-HF, TD-CIS and TD-CIS(D) Approaches. *J. Chem. Phys.* **2007**, *126*, 244110.

(3) Sonk, J. A.; Caricato, M.; Schlegel, H. B. TD-CI Simulation of the Electronic Optical Response of Molecules in Intense Fields: Comparison of RPA, CIS, and EOM-CCSD. *J. Phys. Chem. A* **2011**, *115*, 4678–4690.

(4) Sonk, J. A.; Schlegel, H. B. TD-CI Simulation of the Electronic Optical Response of Molecules in Intense Fields II: Comparison of DFT Functionals and EOM-CCSD. *J. Phys. Chem. A* **2011**, *115*, 11832–11840.

(5) Luppi, E.; Head-Gordon, M. Computation of High-Harmonic Generation Spectra of H_2 and N_2 in Intense Laser Pulses using Quantum Chemistry Methods and Time-Dependent Density Functional Theory. *Molecular Physics* **2012**, *110*, 909–923.

(6) Nguyen, T. S.; Koh, J. H.; Lefelhocz, S.; Parkhill, J. Black-Box, Real-Time Simulations of Transient Absorption Spectroscopy. *J. Phys. Chem. Lett.* **2016**, *7*, 1590–1595.

(7) Nascimento, D. R.; DePrince III, A. E. Modeling molecule-plasmon interactions using quantized radiation fields within time-dependent electronic structure theory. *J. Chem. Phys.* **2015**, *143*, 214104.

(8) Sato, T.; Ishikawa, K. L. Time-dependent Complete-active-space Self-consistent-field Method for Multielectron Dynamics in Intense Laser Fields. *Phys. Rev. A* **2013**, *88*, 023402.

(9) Miyagi, H.; Madsen, L. B. Time-dependent restricted-active-space self-consistent-field theory for laser-drivern many-electron dynamics. *Phys. Rev. A* **2013**, *87*, 062511.

(10) Miyagi, H.; Madsen, L. B. Time-dependent Restricted-active-space Self-consistent-field theory for Laser-driven Many-electron Dynamics. II. Extended Formulation and Numerical Analysis. *Phys. Rev. A* **2014**, *89*, 063416.

(11) Sato, T.; Ishikawa, K. L. Time-dependent Multiconfiguration Self-consistent-field Method Based on the Occupation-restriced Multiple-active-space Model for Multielectron Dynamics in Intense Laser Fields. *Phys. Rev. A* **2015**, *91*, 023417.

(12) Liu, H.; Jenkins, A. J.; Wildman, A.; Frisch, M. J.; Lipparini, F.; Mennucci, B.; Li, X. Time-Dependent Complete Active Space Embedded in a Polarizable Force Field. *J. Chem. Theory Comput.* **2019**, *15*, 1633–1641.

(13) Krause, P.; Klamroth, T.; Saalfrank, P. Time-dependent configuration-interaction calculations of laser-pulse-driven many-electron dynamics: Controlled dipole switching in lithium cyanide. *J. Chem. Phys.* **2005**, *123*, 074105.

(14) DePrince, A. E.; Pelton, M.; Guest, J. R.; Gray, S. K. Emergence of Excited-State Plasmon Modes in Linear Hydrogen Chains from Time-Dependent Quantum Mechanical Methods. *Phys. Rev. Lett.* **2011**, *107*, 196806.

(15) Goings, J. J.; Lestrange, P. J.; Li, X. Real-Time Time-Dependent Electronic Structure Theory. *WIREs Computational Molecular Science* **2018**, *8*, e1341.

(16) Lestrange, P.; Hoffman, R., Mark; Li, X. Time-Dependent Configuration Interaction

Using the Graphical Unitary Group Approach: Nonlinear Electric Properties. *Adv. Quantum Chem.* **2018**, *76*, 295–313.

(17) Ulusoy, I. S.; Stewart, Z.; Wilson, A. K. The role of the CI expansion length in time-dependent studies. *J. Chem. Phys.* **2018**, *148*, 014107.

(18) White, A. F.; Heide, C. J.; Saalfrank, P.; Head-Gordon, M.; Luppi, E. Computation of high-harmonic generation spectra of the hydrogen molecule using time-dependent configuration-interaction. *Mol. Phys.* **2015**, *114*, 947–956.

(19) Cederbaum, L. S.; Zobeley, J. Ultrafast charge migration by electron correlation. *Chem. Phys. Lett.* **1999**, *307*, 205–210.

(20) Kuleff, A. I.; Cederbaum, L. S. Ultrafast Correlation-driven Electron Dynamics. *J. Phys. B* **2014**, *47*, 124002.

(21) Kuleff, A. I.; Cederbaum, L. S. Tracing Ultrafast Interatomic Electronic Decay Processes in Real Time and Space. *Phys. Rev. Lett.* **2007**, *98*, 083201.

(22) Dutoi, A. D.; Cederbaum, L. S.; Wormit, M.; Starcke, J. H.; Dreuw, A. Tracing molecular electronic excitation dynamics in real time and space. *J. Chem. Phys.* **2010**, *132*, 144302.

(23) Bauch, S.; Sørensen, L. K.; Madsen, L. B. Time-dependent generalized-active-space configuration-interaction approach to photoionization dynamics of atoms and molecules. *Phys. Rev. A* **2014**, *90*, 062508.

(24) Crawford-Uranga, A.; De Giovannini, U.; Räsänen, E.; Oliveira, M. J. T.; Mowbray, D. J.; Nikolopoulos, G. M.; Karamatskos, E. T.; Markellos, D.; Lambropoulos, P.; Kurth, S. et al. Time-dependent density-functional theory of strong-field ionization of atoms by soft x rays. *Phys. Rev. A* **2014**, *90*, 033412.

(25) Krause, P.; Sonk, J. A.; Schlegel, H. B. Strong field ionization rates simulated with time-dependent configuration interaction and an absorbing potential. *J. Chem. Phys.* **2014**, *140*, 174113.

(26) Krause, P.; Schlegel, H. B. Angle-Dependent Ionization of Small Molecules by Time-Dependent Configuration Interaction and an Absorbing Potential. *J. Phys. Chem. Lett.* **2015**, *6*, 2140–2146, PMID: 26266516.

(27) Hoerner, P.; Schlegel, H. B. Angular Dependence of Ionization by Circularly Polarized Light Calculated with Time-Dependent Configuration Interaction with an Absorbing Potential. *J. Phys. Chem. A* **2017**, *121*, 1336–1343, PMID: 28098455.

(28) Hoerner, P.; Schlegel, H. B. Angular Dependence of Strong Field Ionization of Haloacetylenes HCCX (X = F, Cl, Br, I), Using Time-Dependent Configuration Interaction with an Absorbing Potential. *J. Phys. Chem. C* **2018**, *122*, 13751–13757.

(29) Tussupbayev, S.; Govind, N.; Lopata, K.; Cramer, J., Christopher Comparison of Real-Time and Linear-Response Time-Dependent Density Functional Theories for Molecular Chromophores Ranging from Sparse to High Densities of States. *J. Chem. Theory Comput.* **2015**, *11*, 1102–1109.

(30) Nascimento, D. R.; DePrince, A. E. A general time-domain formulation of equation-of-motion coupled-cluster theory for linear spectroscopy. *J. Chem. Phys.* **2019**, *151*, 204107.

(31) Bruner, A.; LaMaster, D.; Lopata, K. Accelerated Broadband Spectra Using Transition Dipole Decomposition and Padé Approximants. *J. Chem. Theory Comput.* **2016**, *12*, 3741–3750.

(32) Nascimento, D. R.; DePrince III, A. E. Simulation of Near-Edge X-ray Absorption Fine Structure with Time-Dependent Equation-of-Motion Coupled-Cluster Theory. *J. Phys. Chem. Lett.* **2017**, *8*, 2951–2957.

(33) Kasper, J. M.; Lestrange, P. J.; Stetina, T. F.; Li, X. Modeling $L_{2,3}$-Edge X-ray Absorption Spectroscopy with Real-Time Exact Two-Component Relativistic Time-Dependent Density Functional Theory. *J. Chem. Theory Comput.* **2018**, *14*, 1998–2006.

(34) Kvaal, S. Ab initio quantum dynamics using coupled-cluster. *J. Chem. Phys.* **2012**, *136*, 194109.

(35) Nascimento, D. R.; DePrince III, A. E. Linear Absorption Spectra from Explicitly Time-Dependent Equation-of-Motion Coupled-Cluster Theory. *J. Chem. Theory Comput.* **2016**, *12*, 5834–5840.

(36) Huber, C.; Klamroth, T. Explicitly Time-dependent Coupled Cluster Singles Doubles Calculations of Laser-driven Many-electron Dynamics. *J. Chem. Phys.* **2011**, *134*, 054113.

(37) Sato, T.; Pathak, H.; Orimo, Y.; Ishikawa, K. L. Communication: Time-dependent optimized coupled-cluster method for multielectron dynamics. *J. Chem. Phys.* **2018**, *148*, 051101.

(38) Pathak, H.; Sato, T.; Ishikawa, K. L. Time-dependent optimized coupled-cluster method for multielectron dynamics. II. A coupled electron-pair approximation. *Journal of Chemical Physics* **2020**, *152*, 124115.

(39) Koulias, L. N.; Williams-Young, D. B.; Nascimento, D. R.; DePrince, A. E.; Li, X. Relativistic Real-Time Time-Dependent Equation-of-Motion Coupled-Cluster. *J. Chem. Theory Comput.* **2019**, *15*, 6617–6624.

(40) Manolopoulos, D. E.; Gray, S. K. Symplectic integrators for the multichannel Schrödinger equation. *J. Chem. Phys.* **1995**, *102*, 9214–9227.

(41) Gray, S. K.; Manolopoulos, D. E. Symplectic integrators tailored to the time-dependent Schrödinger equation. *J. Chem. Phys.* **1996**, *104*, 7099–7112.

(42) Sanz-Serna, J. M.; Portillo, A. Classical numerical integrators for wave-packet dynamics. *J. Chem. Phys.* **1996**, *104*, 2349–2355.

(43) Pedersen, T. B.; Kvaal, S. Symplectic integration and physical interpretation of time-dependent coupled-cluster theory. *J. Chem. Phys.* **2019**, *150*, 144106.

(44) Park, Y. C.; Perera, A.; Bartlett, J., Rodney Equation of Motion coupled-cluster for core excitation spectra: Two complementary approaches. *Journal of Chemical Physics* **2019**, *151*, 164117.

(45) Pedersen, T. B.; Kristiansen, H. E.; Bodenstein, T.; Kvaal, S.; Schøyen, Ø. S. Interpretation of Coupled-Cluster Many-Electron Dynamics in Terms of Stationary States. *Journal of Chemical Theory and Computation* **2021**, *17*, 388 – 404.

(46) Neville, S. P.; Schuurman, M. S. A general approach for the calculation and characterization of x-ray absorption spectra. *J. Chem. Phys.* **2018**, *149*, 154111.

(47) Neville, S. P.; Schuurman, M. S. Efficient Solution of the Electronic Eigenvalue Problem Using Wavepacket Propagation. *J. Chem. Theory Comput.* **2018**, *14*, 1433–1441, PMID: 29394052.

(48) Park, T. J.; Light, J. C. Unitary quantum time evolution by iterative Lanczos reduction. *J. Chem. Phys.* **1986**, *85*, 5870.

(49) Stanton, J. F.; Bartlett, R. J. The Equation of Motion Coupled-Cluster Method. A Systematic Biorthogonal Approach to Molecular Excitation Energies, Transition Probabilities, and Excited State Properties. *J. Chem. Phys.* **1993**, *98*, 7029–7039.

(50) Bartlett, R. J. Coupled-cluster theory and its equation-of-motion extensions. *WIREs Computational Molecular Science* **2012**, *2*, 126–138.

(51) Bartlett, R. J.; Musiał, M. Coupled-cluster theory in quantum chemistry. *Rev. Mod. Phys.* **2007**, *79*, 291–352.

(52) Krylov, A. I. Equation-of-Motion Coupled-Cluster Methods for Open-Shell and Electronically Excited Species: The Hitchhiker's Guide to Fock Space. *Annual Review of Physical Chemistry* **2008**, *59*, 433–462.

(53) Coriani, S.; Fransson, T.; Christiansen, O.; Norman, P. Asymmetric-Lanczos-Chain-Driven Implementation of Electronic Resonance Convergent Coupled-Cluster Linear Response Theory. *J. Chem. Theory Comput.* **2012**, *8*, 1616–1628.

(54) Purvis, G. D.; Bartlett, R. J. A Full Coupled-cluster Singles and Doubles Model: The Inclusion of Disconnected Triples. *J. Chem. Phys.* **1982**, *76*, 1910–1918.

(55) Castro, A.; Marques, M. A. L.; Rubio, A. Propagators for the time-dependent Kohn-Sham equations. *J. Chem. Phys.* **2004**, *121*, 3425–3433.

(56) Pueyo, A. G.; Marques, M. A. L.; Rubio, A.; Castro, A. Propagators for the time-dependent Kohn-Sham equations: Multistep, Runge-Kutta, Exponential Runge-Kutta, and Commutator Free Magnus Methods. *J. Chem. Theory Comput.* **2018**, *14*, 3040–3052.

(57) Baer, R.; Neuhauser, D. Real-time linear response for time-dependent density-functional theory. *J. Chem. Phys.* **2004**, *121*, 9803–9807.

(58) Wang, F.; Yam, C. Y.; Chen, G.; Fan, K. Density Matrix Based Time-dependent Density Functional Theory and the Solution of Its Linear Response in Real Time Domain. *J. Chem. Phys.* **2007**, *126*, 134104.

(59) Li, X.; Smith, S. M.; Markevitch, A. N.; Romanov, D. A.; Levis, R. J.; Schlegel, H. B. A time-dependent Hartree-Fock approach for studying the electronic optical response of molecules in intense fields. *Phys. Chem. Chem. Phys.* **2005**, *7*, 233–239.

(60) Kuleff, A. I.; Breidbach, J.; Cederbaum, L. S. Multielectron wave-packet propagation: General theory and application. *J. Chem. Phys.* **2005**, *123*, 044111.

(61) Parrish, R. M.; Burns, L. A.; Smith, D. G. A.; Simmonett, A. C.; DePrince, A. E.; Hohenstein, E. G.; Bozkaya, U.; Sokolov, A. Y.; Di Remigio, R.; Richard, R. M. et al. Psi4 1.1: An Open-Source Electronic Structure Program Emphasizing Automation, Advanced Libraries, and Interoperability. *J. Chem. Theory Comput.* **2017**, *13*, 3185–3197.

(62) Williams-Young, D. B.; Petrone, A.; Sun, S.; Stetina, T. F.; Lestrange, P.; Hoyer, C. E.; Nascimento, D. R.; Koulias, L.; Wildman, A.; Kasper, J. et al. The Chronus Quantum software package. *WIREs Computational Molecular Science* **2020**, *10*, e1436.

(63) Dunning, T. H. Gaussian basis sets for use in correlated molecular calculations. I. The atoms boron through neon and hydrogen. *The Journal of Chemical Physics* **1989**, *90*, 1007–1023.

(64) Woon, D. E.; Dunning, T. H. Gaussian basis sets for use in correlated molecular calculations. III. The atoms aluminum through argon. *The Journal of Chemical Physics* **1993**, *98*, 1358–1371.

(65) Whitten, J. L. Coulombic potential energy integrals and approximations. *J. Chem. Phys.* **1973**, *58*, 4496–4501.

(66) Dunlap, B. I.; Connolly, J. W. D.; Sabin, J. R. On some approximations in applications of X_α theory. *J. Chem. Phys.* **1979**, *71*, 3396–3402.

(67) Pavarini, E.; Koch, E.; Vollhardt, D.; Lichtenstein, A. *The LDA+DMFT approach to strongly correlated materials*; Forschungszentrum Jülich: J¨ulich, Germany, 2011.

(68) Aiem, P.; Bruch, R.; Stolterfoht, N. Autoionization spectra of Li I and Li 11 excited by H+ and He+ impact. *J. Phys. B: At. Mol. Phys.* **1975**, *8*, L480–L484.

(69) Lacombe, S.; Bournel, F.; Laffon, C.; Parent, P. Radical Photochemistry in Oxygen-Loaded Ices. *Angewandte Chemie International Edition* **2006**, *45*, 4159–4163.

(70) Wight, G.; Brion, C. K-shell excitations in NO and O2 by 2.5 keV electron impact. *Journal of Electron Spectroscopy and Related Phenomena* **1974**, *4*, 313 – 325.

(71) Shigemasa, E.; Ueda, K.; Sato, Y.; Sasaki, T.; Yagishita, A. Symmetry-resolved K-shell Photoabsorption Spectra of Free N_2 Molecules. *Phys. Rev. A* **1992**, *45*, 2915–2921.

(72) Schirmer, J.; Trofimov, A. B.; Randall, K. J.; Feldhaus, J.; Bradshaw, A. M.; Ma, Y.; Chen, C. T.; Sette, F. K-shell Excitation of the Water, Ammonia, and Methane Molecules Using High-resolution Photoabsorption Spectroscopy. *Phys. Rev. A* **1993**, *47*, 1136–1147.

(73) Alagia, M.; Lavollée, M.; Richter, R.; Ekström, U.; Carravetta, V.; Stranges, D.; Brunetti, B.; Stranges, S. Probing the potential energy surface by high-resolution x-ray absorption spectroscopy: The umbrella motion of the core-excited CH_3 free radical. *Phys. Rev. A* **2007**, *76*, 022509.

(74) Peng, B.; Lestrange, P. J.; Goings, J. J.; Caricato, M.; Li, X. Energy-Specific Equation-of-Motion Coupled-Cluster Methods for High-Energy Excited States: Application to K-edge X-ray Absorption Spectroscopy. *Journal of Chemical Theory and Computation* **2015**, *11*, 4146 – 4153.

(75) Halbert, L.; Vidal, M. L.; Shee, A.; Coriani, S.; Gomes, A. S. P. Relativistic EOM-CCSD for core-excited and core-ionized state energies based on the 4-component Dirac-Coulomb(-Gaunt) Hamiltonian. 2021.

(76) Cederbaum, L. S.; Domcke, W.; Schirmer, J. Many-body Theory of Core Holes. *Phys. Rev. A* **1980**, *22*, 206–222.

(77) Barth, A.; Schirmer, J. Theoretical Core-Level Excitation Spectra of N_2 and CO by a New Polarisation Propagator Method. *Journal of Physics B: Atomic and Molecular Physics* **1985**, *18*, 867–885.

(78) Coriani, S.; Koch, H. Communication: X-ray Absorption Spectra and Core-Ionization Potentials within a Core-Valence Separated Coupled Cluster Framework. *J. Chem. Phys.* **2015**, *143*, 181103.

(79) Vidal, M. L.; Feng, X.; Epifanovsky, E.; Krylov, A. I.; Coriani, S. New and Efficient Equation-of-Motion Coupled-Cluster Framework for Core-Excited and Core-Ionized States. *J. Chem. Theory Comput.* **2019**, *15*, 3117–3133.

(80) Sonk, J. A.; Caricato, M.; Schlegel, H. B. TD-CI Simulation of the Electronic Optical Response of Molecules in Intense Fields: Comparison of RPA, CIS, CIS(D), and EOM-CCSD. *J. Phys. Chem. A* **2011**, *115*, 4678–4690.

(81) Luppi, E.; Head-Gordon, M. Computation of High-harmonic Generation Spectra of H_2 and N_2 in Intense Laser Pulses using Quantum Chemistry Methods and Time-dependent Density Functional Theory. *Mol. Phys.* **2012**, *110*, 909–923.

(82) Golub, G. H.; van Loan, C. F. *Matrix Computations*; John Hopkins University Press: Baltimore, Maryland, 1996.

(83) Stanton, J. F.; Bartlett, R. J. A coupled-cluster based effective Hamiltonian method for dynamic electric polarizabilities. *J. Chem. Phys.* **1993**, *99*, 5178–5183.

(84) Nanda, K. D.; Krylov, A. I.; Gauss, J. Communication: The pole structure of the dynamical polarizability tensor in equation-of-motion coupled-cluster theory. *J. Chem. Phys.* **2018**, *149*, 141101.

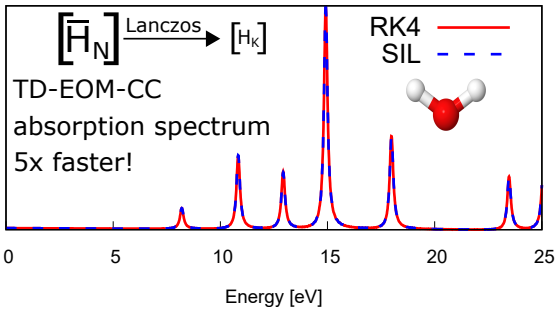

For table of contents only.